



# Fuel Pellet and Rod Thermo-Mechanical Analysis

K M Zaheen Nasir

April 2024

## 1 Introduction

Recent undertakings in the nuclear power engineering community for increasing the life of LWR reactors and their constituents necessitate critical analysis of the prevalent fuel types in terms of their longevity, economy, performance at high burn-up, and temperature. Consequently, thermo-mechanical analysis of LWR fuel is an important stepping stone for analyzing the overall performance of the fuel and its interaction with the surroundings. This is primarily because the fuel's microstructure, integrity, and material properties change due to temperature and burn-up with time. Therefore, starting from the radial temperature distribution of a single pellet, this project sequentially performs thermo-mechanical analysis of a  $UO_2$  fuel rod. The axial variation of the temperature field is also simulated for a single fuel rod.

All three studies were performed in an axisymmetric manner in RZ coordinates. Figure 1 shows the given pellet geometry. The fuel rod has similar fuel, gap, and clad dimensions as the pellet except for the length, which is 1 m. In the case of the pellet, both steady and transient thermal analyses have been performed for constant and temperature-dependent thermal conductivity of fuel and gap. Cladding thermal conductivity was taken as constant in all cases. Initially, for the fuel rod, only steady-state thermal analysis was performed for axially varying heat generation rate and coolant temperature with temperature-dependent thermal conductivity. Finally, a thermo-mechanical simulation is performed to observe the pellet cladding mechanical interaction (PCMI) behavior considering both thermal expansion and irradiation swelling of the fuel with varying temperature fields. Table 1 provides the material-specific thermal, burn-up, and flow parameters considered for these analyses.

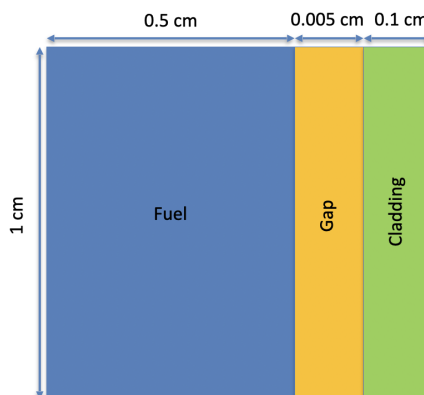


Figure 1: Pellet Geometry in RZ Coordinate (Axisymmetric 2D).

## 2 Meshing

### 2.1 Pellet Geometry

The given geometry was meshed using the **GeneratedMeshGenerator** moose object. For the steady state analyses, we adopted a 1000 x 1000 elements mesh initially along R and Z directions respectively. Afterward, a convergence study showed that similar results can be achieved through a more coarse mesh of 125 x 125 elements within 1.5% error. Therefore, a mesh of 125 x 125 was used for the sake of alacrity in moving forward. Although a good FEM analysis requires a balanced aspect ratio for each element's dimensions, the same number of elements in each dimension were used for this simple geometry without increasing the element number in Z direction. Moose object **SubdomainBoundingBoxGenerator** were used to further subdivide the domain

Quantity	Symbol	Value/Function
Outer Cladding Temperature	$T_{CO}$	550 K (pellet)
Fuel Thermal Conductivity Constant	$K_F$	$0.03 \text{ W}/(\text{cm} * \text{K})$
Fuel Thermal Conductivity Temp Dependent	$K_{FT}$	$K_{FT} = 1/(A + BT)$ , $A = 3.8 + 200 * FIMA$ , $B = 0.0217$
Gap Thermal Conductivity Constant	$K_g$	$0.002556 \text{ W}/(\text{cm} * \text{K})$
Gap Thermal Conductivity Temp Dependent	$K_{gT}$	$(16 * 10^{-6}) * T^{0.79} \text{ W}/(\text{cm} * \text{K})$
Cladding Thermal Conductivity	$K_C$	$0.17 \text{ W}/(\text{cm} * \text{K})$
LHR Steady	$LHR/LHR^o$	$350 \text{ W/cm}$
LHR Transient	$LHR$	$250 * \exp(-((t - 20)^2)/10) + 150 \text{ W/cm}$
Coolant Flow rate	$\dot{m}$	$0.05 \text{ Kg/s} - \text{rod}$ (a smaller value is taken to observe the effect of peak shifting) $0.25 \text{ Kg/s} - \text{rod}$ (for thermo-mechanical simulations)
Coolant Inlet Temperature	$T_{cool}^{in}$	500 K
Burn-up	$\beta$	0.00295 FIMA (reduced to compensate for increased thermal expansion co-efficient)

Table 1: Material Specific Thermal, Burn-up and Flow Parameters for Fuel Pellet and Rod

into three blocks representing fuel, gap, and cladding. Figure 2 shows the subdivisions of the problem domain. An element number of 125 is chosen in the R direction so that the element size (0.00484 cm) remains smaller than the gap width and the mesh object can easily recognize the gap block. However, any element size smaller than the gap size would've also worked. Similarly, we maintained the same number of elements for transient analyses as well.

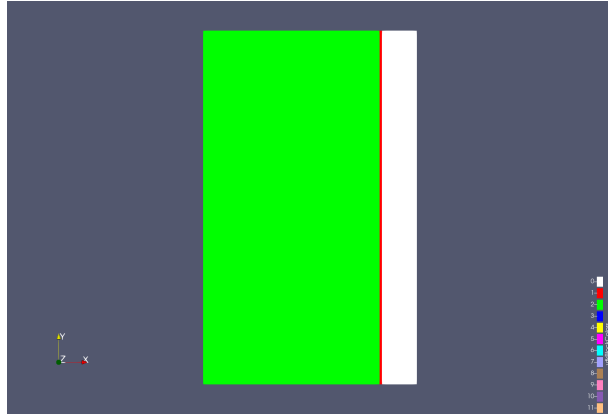


Figure 2: Mesh blocks representing fuel(Green), gap(red), cladding(white).

## 2.2 Rod Geometry

### 2.2.1 Thermal analysis

We adopted a similar approach mentioned in section 2.1 to create the initial rod geometry and mesh. Thereafter, we used **SideSetsBetweenSubdomainsGenerator** to generate and name the boundaries between fuel and gap as well as clad and gap respectively. To properly utilize the **GapHeatTransfer** under **ThermalContact** which calculates the heat transfer across an unmeshed gap, we also deleted the gap block using **BlockDeletionGenerator**. A slice of rod mesh blocks are shown in Figure 3. A convergence study was performed to determine the optimum number of elements for faster calculation with reasonable accuracy of axial variation. The study investigated starting from as little as 125 elements in either dimension up to 1500 elements. The impact of aspect ratio on the results was also investigated using **nx = 125 (R)** and **ny = 1500 (Z)** elements. No effect of aspect ratio was observed on the results. Also, a variation of only 3% was observed between the most refined and coarse mesh. Therefore, a mesh of 125 x 125 was finally adopted for these analyses. Table 2 lists the results of the convergence study for the axial variation of the temperature profile.

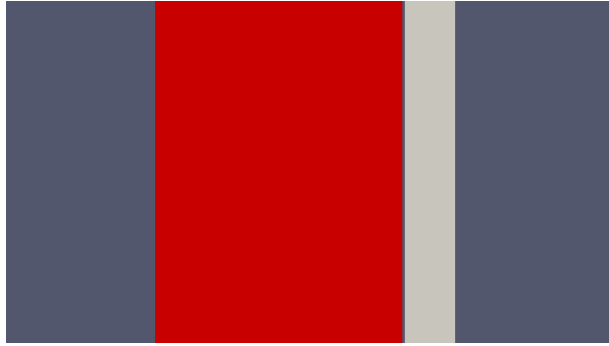


Figure 3: A slice of rod mesh blocks representing fuel (red) & cladding (gray) with unmeshed gap.

Mesh Size (x by y)	T(z=0m)	$T_{max}(z = 0.534m)$	T(z=1m)
125 x 125	790.128	1670.05	952.49
250 x 250	793	1680	957.549
500 x 500	792.42	1675.37	953.422
1000 x 1000	804.443	1722.14	966.73
1000 x 1500	804.46	1722.14	966.747
125 x 1500	791.485	1670.06	953.58

Table 2: Results of Convergence Study (Temperatures in K).

### 2.2.2 Thermo-mechanical analysis

While the earlier geometry remained the same, the mesh was redefined to observe the PCMI behavior more accurately. Both fuel and clad blocks including boundaries were defined separately and later on, combined using **MeshCollectionGenerator**. Although a good aspect ratio is most desired for the successful simulation of mechanical and contact problems, a mesh size of 125 x 1000 and 26 x 1000 was maintained within the fuel and cladding blocks respectively for faster convergence of the transient simulations using reasonable computational resources at our disposal. We refrained from doing a thorough convergence study as the mesh used was already coarse enough with expected mechanical behavior. On the other hand, a more finer mesh would result in a significant addition of computation time.

## 3 Kernels, Variables and Boundary Conditions

Thermal analyses of the fuel pellet and rod were done using the basic heat conduction equation as the governing equation over the respective problem domain. The strong and weak forms of the governing equations are presented below.

**Strong Form:**

$$\rho C_p \frac{\partial T}{\partial t} = \nabla \cdot (k \nabla T) + Q \quad (1)$$

where  $\rho$  is the density,  $C_p$  is the specific heat,  $T$  represents the temperature profile of the fuel pellet and  $Q$  is the heat source.

**Weak Form:**

$$(\phi_i, \rho C_p \frac{\partial T}{\partial t}) + (\nabla \phi_i, k \nabla T) - \langle \phi_i, k \nabla T \cdot \mathbf{n} \rangle + (\phi_i, Q) = 0 \quad (2)$$

where  $\phi_i$  is the FEM weighting or trial function and  $\mathbf{n}$  is the outward vector normal to the boundary. We obtain equation 2 (weak form) from the strong form of the heat conduction equation as per Galerkin formulation where the trial functions are the same as the FEM shape functions. Observing the weak form we automatically understand that the MOOSE implementation requires three kernels for transient analysis for the terms shown within the parenthesis in Equation 2. The number of required kernels is reduced to two for steady-state analyses. We chose **HeatConduction**, **HeatSource**, and **SpecificHeatConductionTimeDerivative** as the kernels of the said thermal analyses. Standard formulations were used to convert **LHR** to heat source **Q** as an input to the **HeatSource** kernel.

The weak form also reveals the necessity of Neuman BC represented by the term within the angular brackets. On the other hand, Dirichlet BCs are directly implemented within the FEM shape function. Therefore, we apply

Neuman BC of  $\nabla T = 0$  on the left boundary representing the centerline of the fuel and  $T = 550$  K on the right boundary as cladding outer temperature for the pellet thermal analyses. The scalar variable temperature is taken as the primary variable representing our required solution field.

For the fuel rod, the **LHR** and coolant temperature also vary axially. This necessitates the use of **FunctionDirichletBC** at the right boundary along with a function implementation within the **HeatSource**. The axial variation of the **LHR** and coolant temperature,  $T_{cool}$  can be captured by the following functions.

**LHR:**

$$LHR(z) = LHR^o \cos\left[\frac{\pi}{2\gamma}\left(\frac{z}{z_o} - 1\right)\right] \quad (3)$$

where  $z_o = 0.5m$  is the fuel midpoint.

**$T_{cool}$ :**

$$T_{cool} = T_{cool}^{in} + \frac{2\gamma}{\pi} \frac{z_o \cdot LHR^o}{\dot{m} \cdot C_p} \left[ \sin\frac{\pi}{2\gamma} + \sin\frac{\pi}{2\gamma}\left(\frac{z}{z_o} - 1\right) \right] \quad (4)$$

Functions were created using **ParsedFunction** object. We chose a value of 0.5 Kg/s-rod for the flow rate to observe the peak shifting of the fuel temperature. Although the value deviates from the ideal scenario, it was needed to observe the peak shifting phenomenon for this smaller-than-ideal system. A  $\gamma$  value of 1.2 was used for the analysis considering extrapolation distance. The **GapHeatTransfer** under **ThermalContact** module was used to transfer the heat across the gap between fuel and cladding.

Simulating thermo-mechanical behavior required us to add the Cauchy momentum equation to the system as the governing equation of mechanics problem to be solved as follows.

$$\rho \mathbf{u}_{i,tt} = \boldsymbol{\sigma}_{ij,j} + f_i \quad (5)$$

where,

$$\boldsymbol{\sigma}_{ij} = \mathbf{C}_{ijkl} \mathbf{u}_{k,l}$$

However, derivation of the weak form to determine the kernels was not required as most of the heavy lifting was done by the **Physics** modules. The addition of displacement variables, kernels, and enforcement of common boundaries was done using **Physics** modules through moose action systems. We also used the **Contact** module to analyze the PCMI behaviors by observing penetration between master and slave surfaces. We chose the fuel surface as the master and the cladding surface as the slave respectively. Simulating the contact requires the tracking of displaced mesh. Therefore, a Total Lagrangian formulation of **FINITE** strain was used to solve the mechanics counterpart of the coupled multi-physics problem. Consequently, a Total Lagrangian formulation of the strain required us to solve the system in a transient manner with coupled **SpecificHeatConduction-TimeDerivative** kernel. Therefore, the system was solved up to a steady state for both axially varying and constant **LHR**. In this regard, we used **steady\_state\_detection=true** to monitor the Steady-State Relative Differential Norm. In order to observe the PCMI, slightly increased thermal expansion coefficients were used for both fuel and cladding materials to account for thermal expansion via **ComputeThermalExpansionEigenstrain**. As compensation, we also used a reduced burn-up for our swelling models. While Densification was ignored to observe more pronounced contact, swellings due to both solid and gaseous fission products were considered using **ComputeVolumetricEigenstrain** based on the material property defined by **ParsedMaterial** given according to the following equations.

Solid fission product swelling:

$$\epsilon_{sfp} = 5.577 \times 10^{-2} \rho \beta \quad (6)$$

Gaseous fission product swelling:

$$\epsilon_{gfp} = 1.96 \times 10^{-28} \rho \beta (2800 - T)^{11.73} e^{-0.0162(2800-T)} e^{-17.8\rho\beta} \quad (7)$$

For displacement boundary conditions, we fix the **translation along the y-axis** to remove rigid body motions for the fuel rod and apply symmetry boundary conditions along the fuel center line to solve for the Cauchy equation of motion.

## 4 Choice of Materials

Our analyses were strictly kept within the LWR scenario. As a result, we chose  $UO_2$  as our fuel material with Zircaloy-4 cladding. Helium is taken as the gas occupying the gap between fuel and cladding material for part one of this project. Naturally, we used water as a coolant for our simulations. Their material properties used in the simulations except for thermal conductivity (already given in table 1) are listed in table 3. These values were taken from the Lecture 3 and 12 slides of the Nuclear Fuel Performance course. As FEM uses consistent units, a pressure unit of  $10^4 \times Pa$  is applied in the input file against a consistent length unit of cm.

Properties	$\text{UO}_2$	He	Zircaloy-4	$\text{H}_2\text{O}$	Units
Density	10.98	$0.178 * 10^{-3}$	6.5	-	$\text{g}/\text{cm}^3$
Specific Heat	0.33	5.188	0.35	4200	$\text{J}/\text{g} - \text{K}$
Thermal Expansion Co-efficient	$11 \times 10^{-5}$	-	$11 \times 10^{-5}$	-	$1/\text{K}$
Poisson's Ratio	0.32	-	0.37	-	-
Young's Modulus	175	-	99	-	$\text{GPa}$

Table 3: Material properties used for the Analyses.

## 5 Results

### 5.1 Pellet Radial Thermal Analysis

Considering helium in the gap we obtained the following analytical solution for the steady state.

$$\frac{\text{LHR}}{2\pi R_F} = \frac{350}{2\pi 0.5} = 111.408$$

Cladding inner temperature:

$$\therefore T_{CI} = T_{CO} + \frac{\text{LHR} \cdot t_c}{2\pi R_F \cdot K_C} = 550 + 111.408 \frac{0.1}{0.17} = 615.534 \text{ K}$$

Assuming  $T_{CI} = T$  we have,

$$K_g = 16 * 10^{-6} * T^{0.79} = 0.002556 \text{ W}/(\text{cm} \cdot \text{K})$$

$$h_{gap} = \frac{K_g}{t_g} = \frac{0.002556}{0.005} = 0.5112 \text{ W}/(\text{cm}^2 \cdot \text{K})$$

Fuel surface temperature:

$$\therefore T_S = T_{CI} + \frac{\text{LHR}}{2\pi R_F \cdot h_{gap}} = 615.534 + \frac{111.408}{0.5112} = 833.46 \text{ K}$$

Fuel centerline temperature:

$$\therefore T_o = T_S + \frac{\text{LHR}}{4\pi K_F} = 833.46 + \frac{350}{4\pi 0.03} = 1761.86 \text{ K}$$

The results of the analyses along with the comparison of steady state solution with our analytical one are portrayed in table 4.

Properties	Steady-Const. K	% Error	Steady-Temp. dep. K	Transient-Const. K	Transient-Temp. dep. K
Fuel centerline temp.(K)	1772.35	0.595	1642.95	1073.88	925.843
Fuel surface temp.(K)	844.943	1.378	818.943	676.407	675.377
Cladding inner temp.(K)	609.023	1.058	609.023	575.296	575.296
Cladding outer temp.(K)	550	0	550	550	550
Approach to steady state (sec)	-	-	-	50	45
Steady-state reached (sec)	-	-	-	85	72

Table 4: Analyses results and comparison with analytical solution.

The contour plots and the spatial profiles of temperature along the radial direction of the fuel pellet including gap and cladding for both constant and temperature-dependent thermal conductivity of the steady state analyses are presented in figure 4 and 5 respectively.

Similar plots including the temporal profile of fuel centerline temperature up to 100 sec for both constant and temperature-dependent thermal conductivity are shown in figure 6 and 7 respectively.

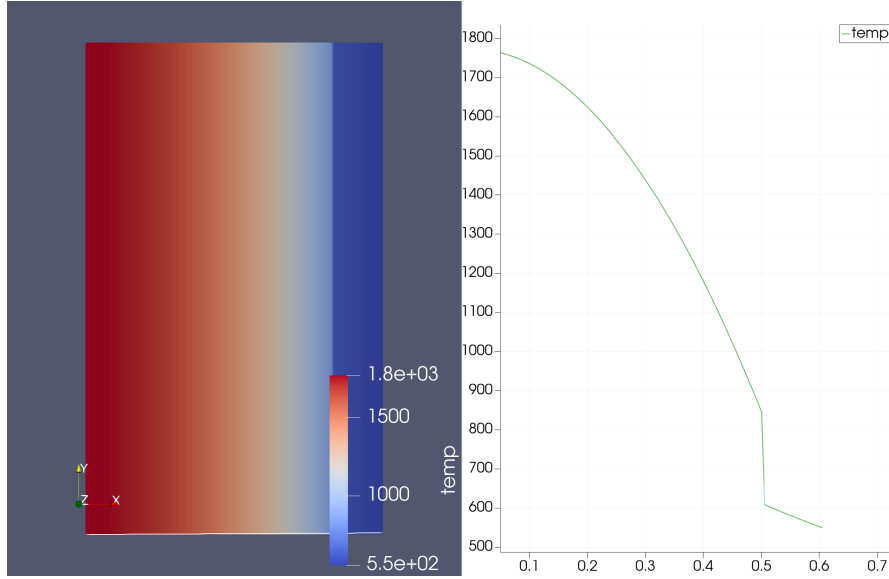


Figure 4: Contour and spatial temperature profile for constant thermal conductivity in steady state.

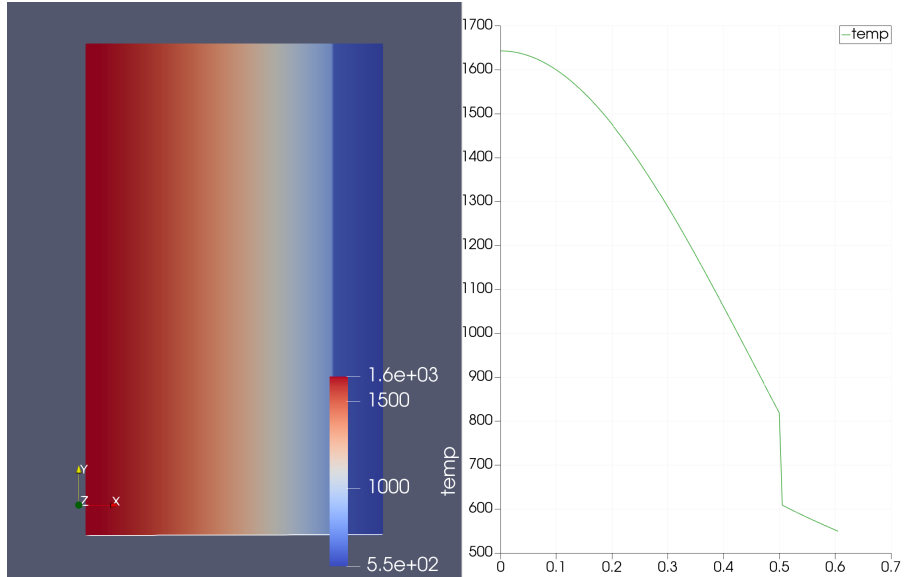


Figure 5: Contour and spatial temperature profile for temperature-dependent thermal conductivity in steady state.

## 5.2 Rod Axial Thermal Analysis

The radial temperature distribution of the fuel rod at  $z=0.25\text{m}$ ,  $z=0.5\text{m}$ , and  $z=1\text{m}$  are presented in the table 5. The temperature profiles are shown in figure 8, 9, 10 respectively.

Temperatures (K)	$T(z=0.25\text{m})$	$T(z=0.5\text{m})$	$T(z=1\text{m})$
Fuel Centerline	1340.14	1665.04	950.91
Fuel Surface	747.71	833.94	728.03
Cladding Inner	573.99	623.46	650.96
Cladding Outer	525.51	564.72	629.45

Table 5: Radial temperature profiles at various heights along the rod.

Due to the reduced flow rate, the peak fuel centerline temperature of 1670.06 K is observed at 53.5 cm. However, a peak fuel surface temperature of 842.761 is found at 60.8 cm as expected. The axial variations of temperatures are presented in figure 11 and 12 respectively.

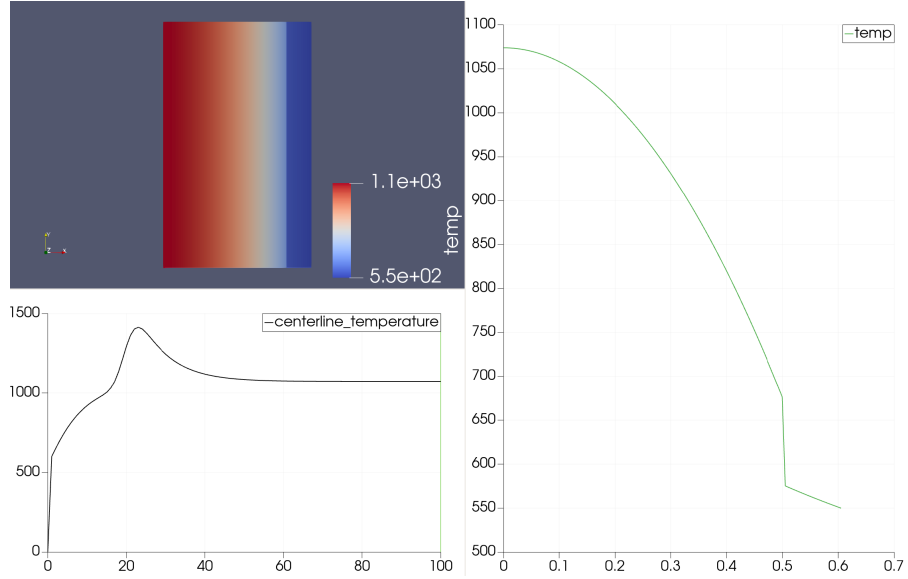


Figure 6: Contour, spatial temperature, and temporal fuel centerline temperature profile for constant thermal conductivity.

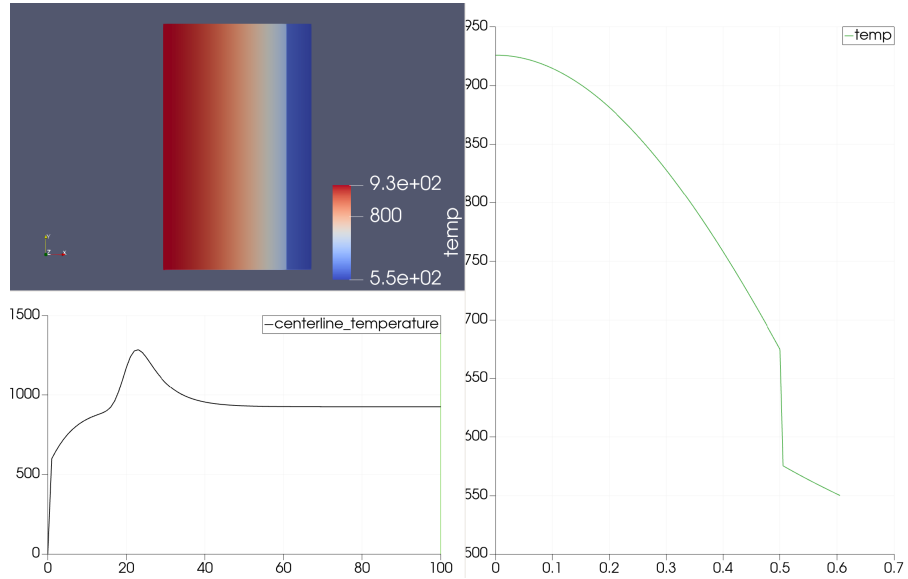


Figure 7: Contour, spatial temperature, and temporal fuel centerline temperature profile for temperature-dependent thermal conductivity.

### 5.3 Rod Thermo-Mechanical Analysis

A comparison between important thermo-mechanical properties summarizing the results of both constant and axially varying **LHR** are provided in table 6. Both analyses were performed considering axially varying outer cladding temperatures.

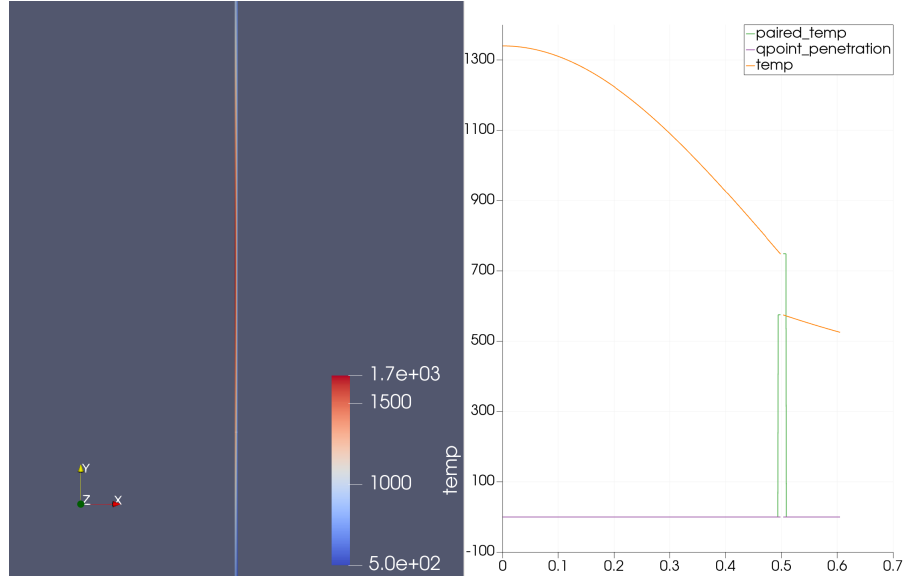


Figure 8: Temperature profile at  $z=0.25$  m.

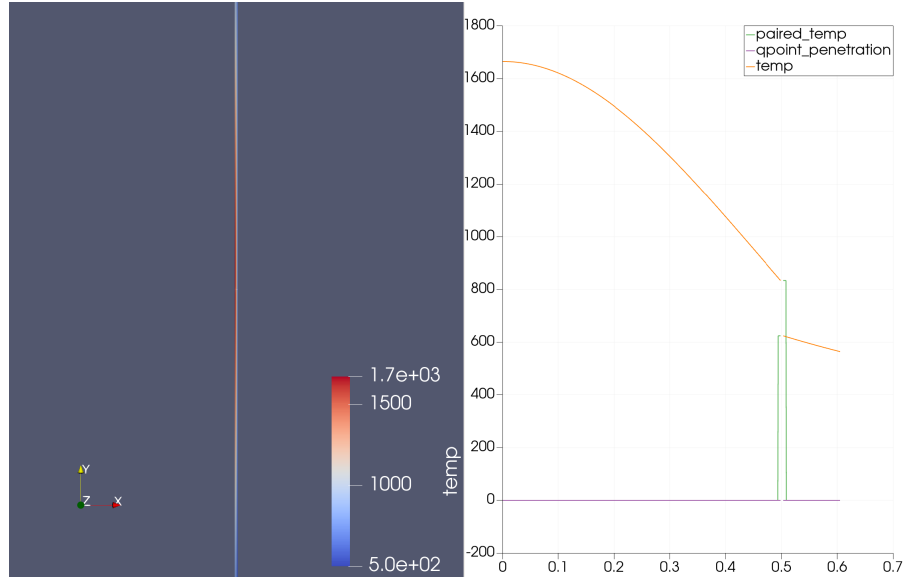


Figure 9: Temperature profile at  $z=0.50$  m.

Properties	Const. LHR	Varying LHR
Peak Fuel centerline temp.(K) & height (cm)	1213.78 at 100	1218.41 at 51
Maximum Von-Mises Stress along Fuel Centerline (Gpa) & height (cm)	21.2 at 0.5	19.55 at 50.2
Maximum Von-Mises Stress along Fuel surface (Gpa) & height (cm)	14.5 at 0	12.8 at 50.2
Displacement Peaks along Fuel Surface & height (cm)	0.089897 at 50.5	0.137249 at 44.5 & 0.082199 at 59 (twin peaks)
$Strain_{xx}$ & height (cm)	0.068620 at 99.9	0.064958 at 46.9 & 0.065449 at 56.5 (twin peaks)
PCMI (contact region)	50 - 99.7	44.7 - 59
Increase in rod radius (cm)	0.06516	0.06356

Table 6: Analyses results and comparison between constant and axially varying LHR.

The axial and radial profile at the height of peak fuel center-line temperature for both constant and axially

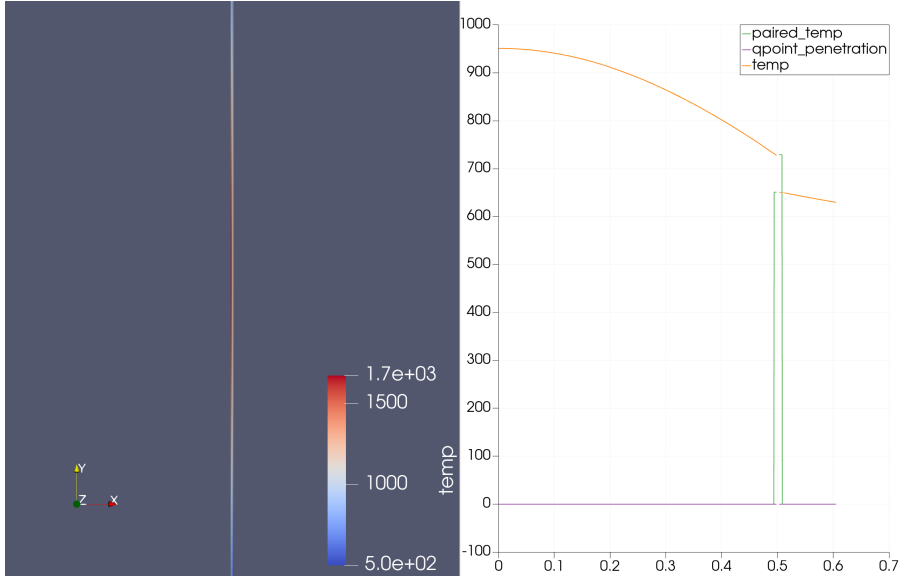


Figure 10: Temperature profile at  $z=1$  m.

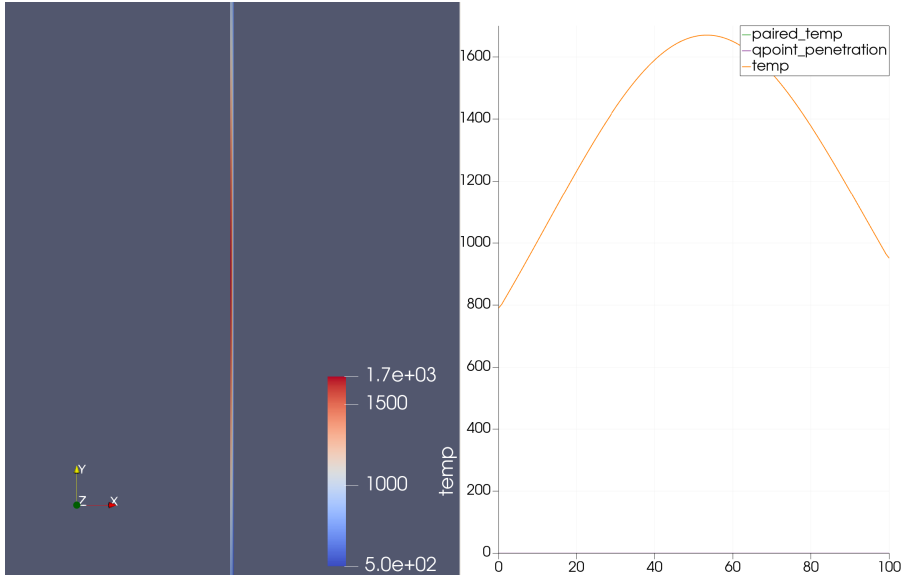


Figure 11: Axial profile of fuel centerline temperature.

varying simulations are shown in figure 13 and 14 respectively. Distributions of effective Von-Mises stress, penetration, displacement, and  $\text{strain}_{xx}$  along fuel surface for both constant and axially varying analyses at steady state are portrayed in figure 15 and 16 sequentially.

## 6 Discussion

In the case of pellet thermal analyses, comparison with the analytical solution for the steady state reveals negligible errors and points towards successful modeling of the fuel pellet temperature profile. According to our empirical dependence of thermal conductivity upon temperature as used in the simulation, fuel thermal conductivity decreases with increasing temperature while gap conductivity increases. However, as observed from our analysis, this had an overall effect of decreasing the fuel centerline temperature resulting in a lower thermal gradient across the fuel pellet compared to constant thermal conductivity. During the transient analyses, it was observed that the nonlinear solve fails to converge when the steady state is approached. This is because the nonlinear Newton-Raphson fails to find a suitable value for the scalar variable temperature that minimizes the residual beyond the set tolerance. The fact that the temperature doesn't deviate much due to the approaching steady state contributes to the inability of Newton-Raphson to minimize the residual beyond a certain value. This problem required a workaround by changing the nonlinear tolerances in the executioner block. We set **nl\_rel\_tol = 1e-10** and **nl\_abs\_tol = 1e-10** to obtain our transient solution. Transient analysis showed a

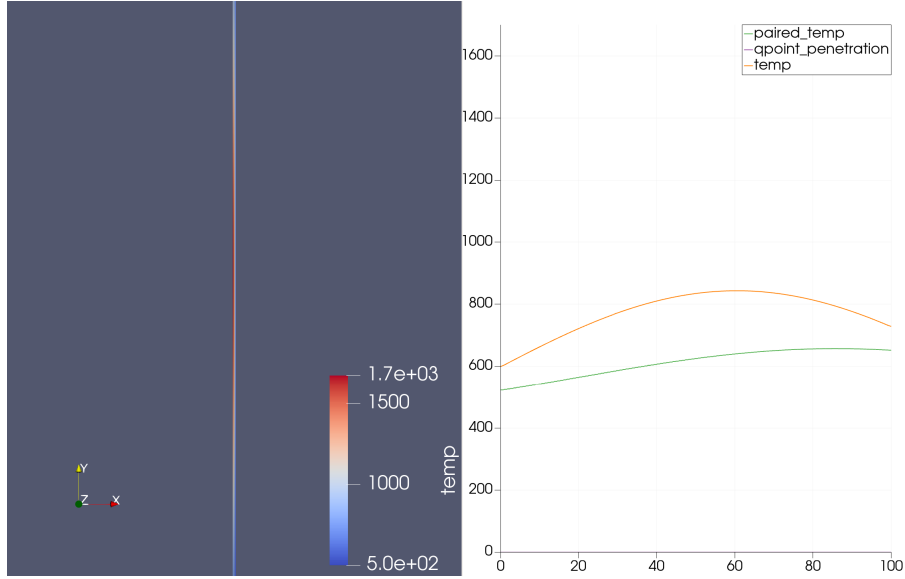


Figure 12: Axial profile of fuel surface temperature.

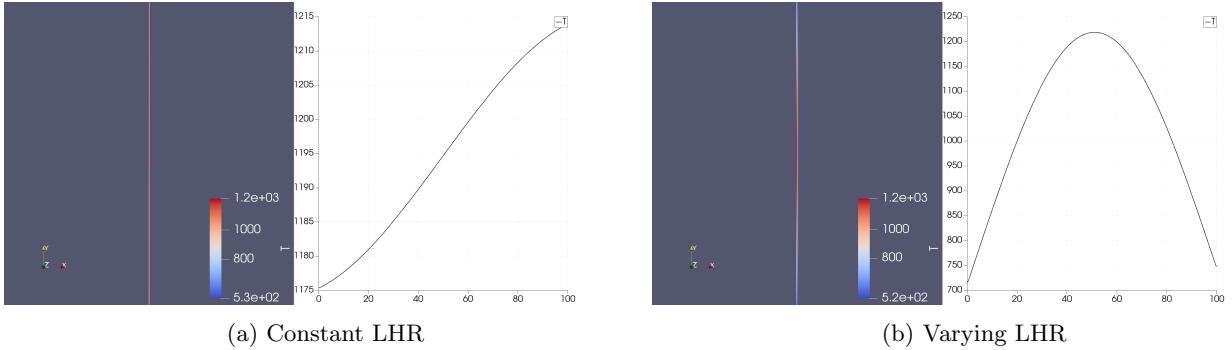


Figure 13: Axial temperature distribution along fuel center-line.

peaking of the fuel centerline temperature at 23 sec reaching 1414.15 K and 1285.82 K for constant and temperature dependent thermal conductivity before reaching respective steady state. We used a post-processor object of **SideExtremeValue** to track the fuel centerline temperature.

For the rod thermal analyses, the temperature profiles obtained for various positions along the fuel rod are in reasonable agreement with the analytical solutions. In ideal cases, maximum fuel centerline temperature occurs around 60% of the fuel length. The maximum heat generation takes place at the midpoint of the fuel height. However, as the comparatively colder coolant moves upward through the channels between the fuel, it gradually becomes hotter by absorbing heat from the fuel rod. Which in turn shifts the peak centerline temperature towards the top. Nevertheless, our given system is significantly smaller than the ideal to observe this peak at the said height. Therefore, with a reduced flow rate as mentioned earlier, we were able to observe the shifted peak at 53.5 cm for the fuel centerline temperature. The phenomenon of peak shifting is more pronounced in the case of the fuel surface temperature. We found the peak fuel surface temperature at 60.8 cm. The use of **GapHeatTransfer** resulted in insignificant variations in the temperature profile compared to the thermal analyses for the pellet.

In the case of thermo-mechanical analyses, a more ideal flow rate is chosen in order to evenly distribute the thermal expansion instead of a reduced flow rate. However, as mentioned before, for this smaller-than-ideal system, slightly increased co-efficient of thermal expansions were used for both the cladding and fuel to observe the contact or PCMI behavior. Consequently, we observed full closure of gaps for both constant and axially varying LHR from the radial temperature profiles. However, we observe different penetration (PCMI) regions for both analyses. While PCMI occurs between 50 to 99.7 cm for the constant LHR, it is found to be within 44.7 to 59 cm in case of varying LHR. A penetration value above zero can only be interpreted as contact or interaction. These findings agree well with the axial temperature distribution along the fuel center line for both cases. For constant LHR, as the cold coolant moves upward it loses the ability to cool the fuel effectively by absorbing heat. This results in a higher temperature towards the top of the fuel rod and in turn more expansion towards the top. This is also evident from the strain along the x-axis at the fuel surface. As a result, PCMIs are

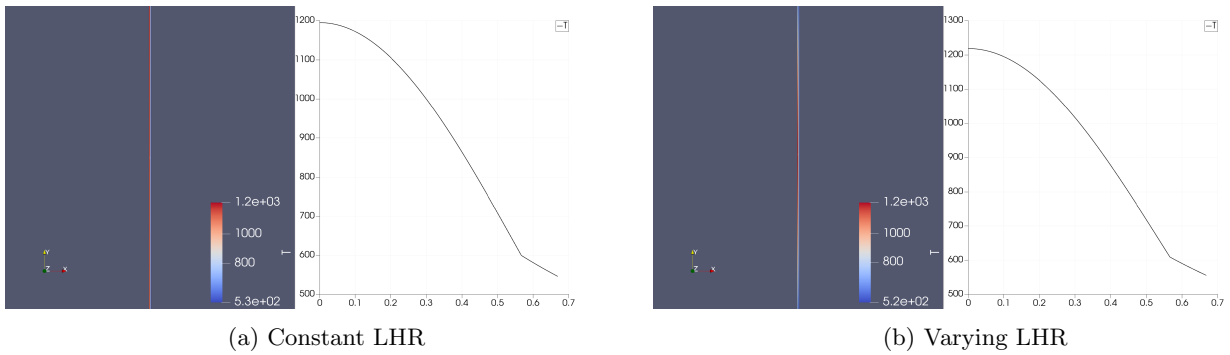


Figure 14: Radial temperature distribution at the height of peak fuel center-line temperature.

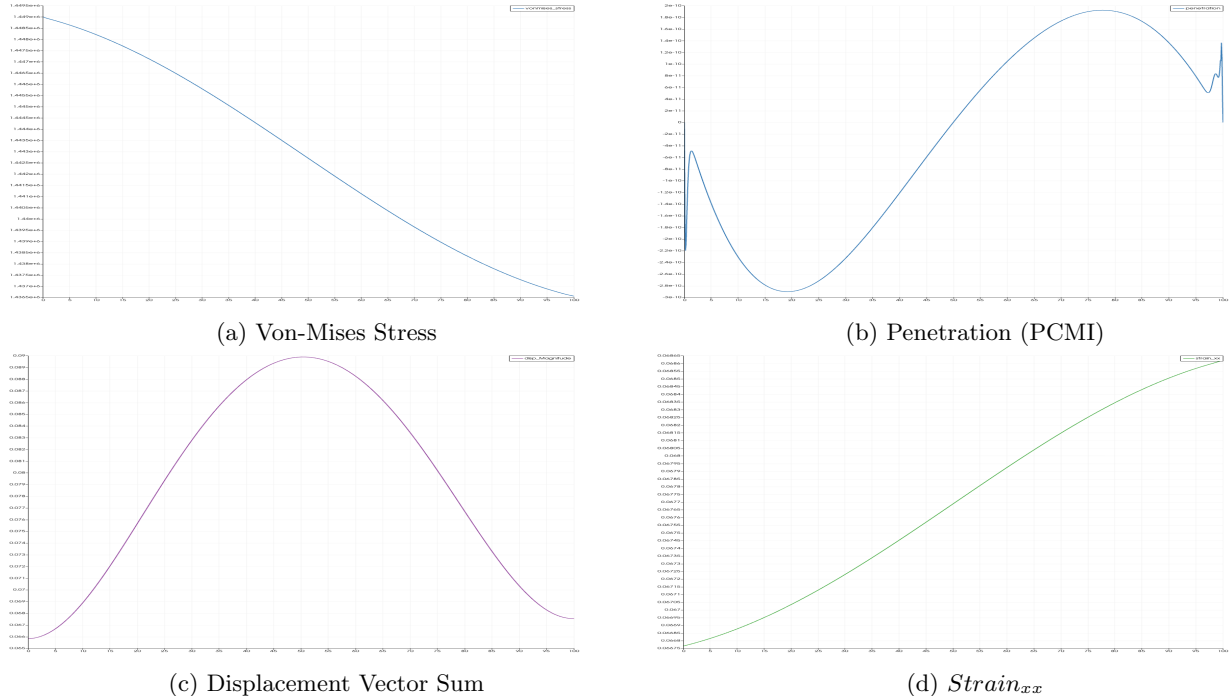


Figure 15: Distributions along fuel surface for Constant LHR

also observed above the fuel height of 50 cm. Similarly, we observe penetration around the hotter middle region of the fuel rod for axially varying LHR (more realistic scenario). In contrast to temperature-dependent gaseous fission product swelling, expansion due to solid fission products contributes uniformly. However, their combined contribution was found significantly less than the thermal expansion for both analyses. Frictionless mortar formulation was used for modeling PCMI for our system. This required us to carefully select the **c\_normal** for getting a convergent solution. Considering the multi-physics coupling and usage of a number of modules, a slightly reduced tolerance of **nl\_rel\_tol = 1e-06** was used to reach a steady state. Additionally, because of a diverse range of solution variables, applying **automatic\_scaling = true** was found essential for obtaining a convergent solution. Numerous trials and errors for reaching a convergent solution approaching a steady state showed that aspect ratio plays an important role in simulating contact problems. Simulating an entire rod for a contact problem requires a well-defined mesh. An ill-posed mesh can lead to highly distorting elements resulting in divergent solutions. We also utilized the **Constraints** action to simulate the thermal contact instead of using **GapHeatTransfer** for these analyses.

7 Conclusion

Accomplishing this project has equipped us with hands-on knowledge for modeling the thermo-mechanical behavior of pellets and rods using MOOSE to solve multi-physics governing equations in a fully coupled way. Although MOOSE is a powerful modular and pluggable framework for performing a wide range of analyses, a thorough understanding of physics behind the problem and numerical schemes such as FEM, implicit time integration using Newton-Raphson or Preconditioned Jacobian Free Newton Krylov (PJFNK), etc in solving

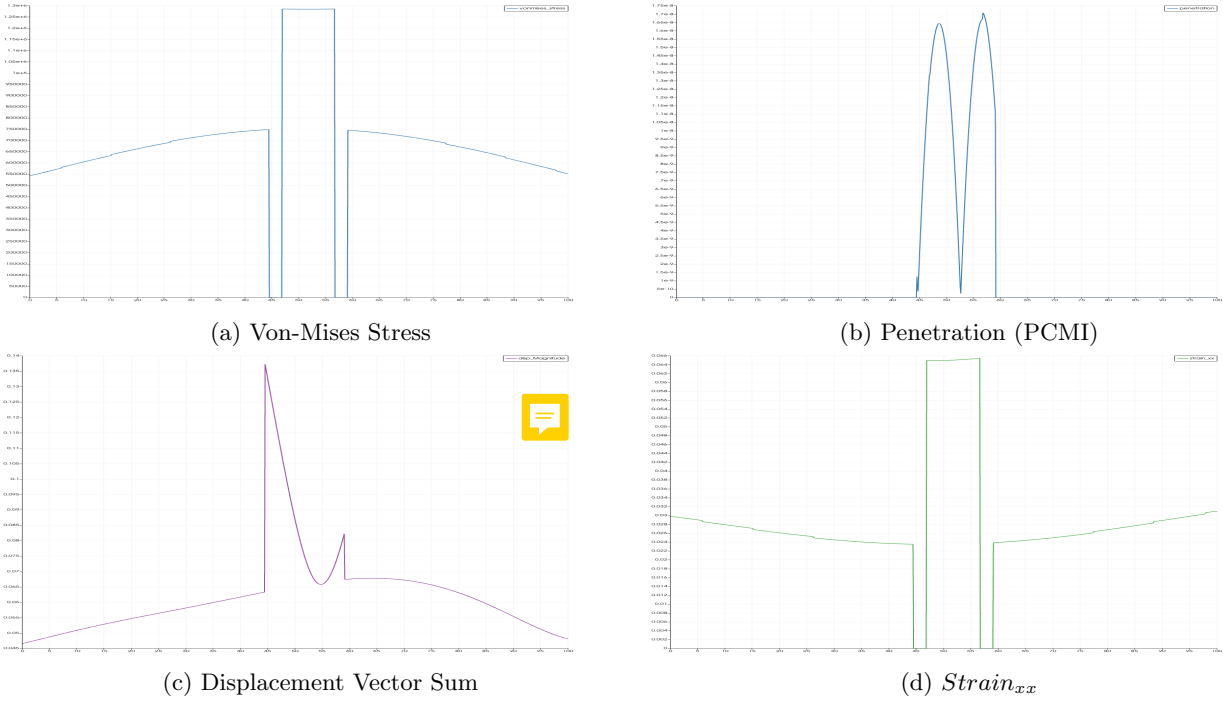


Figure 16: Distributions along fuel surface for axially varying LHR

the problem is essential. Obtaining a transient solution by tweaking the tolerances that don't deviate from the expected behavior according to the physics of the problem domain is a testament to this requirement. Additionally, a grasp on versatile powerful modules and action systems like **Physics\SolidMechanics**, **Contact** and **GapHeatTransfer** will lead to simulations with a significant reduction of efforts. Eventually, these will allow us to perform any kind of large-scale analysis using MOOSE or any type of modeling tool similar to MOOSE.